




Anomalous Hall effect and topological Hall effect in the noncollinear antiferromagnet $V_{0.3}\text{NbS}_2$ Huan Wang ^{1,2}, Xiao-Ping Ma,^{1,2} Xiang-Yu Zeng,^{1,2} Jing Gong,^{1,2} Jun-Fa Lin,^{1,2} Xiao-Yan Wang,^{1,2} Zheng-Yi Dai,^{1,2} Kun Han,^{1,2} Yi-Ting Wang,^{1,2} and Tian-Long Xia ^{1,2,3,4,*}¹*Department of Physics, Renmin University of China, Beijing 100872, People's Republic of China*²*Beijing Key Laboratory of Opto-electronic Functional Materials & Micro-nano Devices, Renmin University of China, Beijing 100872, People's Republic of China*³*Key Laboratory of Quantum State Construction and Manipulation (Ministry of Education), Renmin University of China, Beijing 100872, China*⁴*Laboratory for Neutron Scattering, Renmin University of China, Beijing 100872, People's Republic of China* (Received 22 November 2022; revised 14 February 2023; accepted 14 April 2023; published 27 April 2023)

The recent discoveries of large anomalous Hall effect (AHE) in antiferromagnets (AFMs) have brought intense study in theories and experiments. Special attention has also been given to the topic of topological Hall effect (THE). Both of them provide a good platform for understanding the interplay between magnetism and transport characteristics. Here, we report the magnetic and electrical transport properties of a layered AFM $V_{0.3}\text{NbS}_2$ single crystal. It orders antiferromagnetically below $T_{N1} \sim 53$ K and exhibits weak magnetic hysteresis loop with a tiny net magnetization ($\approx 16 m\mu_B/V$) along the c axis as a result of canted antiferromagnetic configuration. Of particular interest is the realization of AHE in such AFMs with a near-perfect cancellation of moment, which probably originates from the contribution of nonzero Berry curvature. THE is detected at low temperatures, which acts as the probe of spin reorientation in the magnetization process induced by field. The magnetoresistance shows a weak irreversible behavior near zero field, consistent with the hysteresis loop in magnetization and Hall resistivity. It presents a negative value below 7 T, which is ascribed to the spin-dependent scattering. The observation of anomalous transport in $V_{0.3}\text{NbS}_2$ serves as a platform for studying AHE within AFMs.

DOI: [10.1103/PhysRevB.107.134436](https://doi.org/10.1103/PhysRevB.107.134436)**I. INTRODUCTION**

The study of anomalous Hall effect (AHE) in ferromagnets (FMs) has blossomed over the past decades and the continuous expansion of material candidates is regularly fed by the predictions [1–4]. As a result related to spin-orbit coupling (SOC), two mechanisms have been identified for AHE, intrinsic contribution from Berry curvature or extrinsic ones, including skew-scattering and side-jump scattering [5]. In fact, AHE is not limited to FMs. It can also be observed in antiferromagnets (AFMs) with noncoplanar or noncollinear spin structures [6,7] as a result of nonzero Berry curvature in momentum space when certain common symmetries are absent [8–11]. This groundbreaking view has been confirmed in experimental work on AFMs, such as Mn_3X ($\text{X} = \text{Ga}, \text{Ge}, \text{Sn}, \text{Ir}, \text{Pt}$) [12–17], Mn_5Si_3 [18,19], and $\text{Co}_{1/3}\text{NbS}_2$ [20–22], or materials with a complex spin structure, such as $\text{Pr}_2\text{Ir}_2\text{O}_7$ [23] and $\text{Nd}_2\text{Mo}_2\text{O}_7$ [24]. In addition to AHE, topological Hall effect (THE) [25–28] is proposed as another anomalous transport property, which stems from the inhomogeneity of spin texture that yields a Berry phase in real space acting as an associated fictitious magnetic field. It is generated even without SOC, which is usually expected and observed in noncollinear/noncoplanar AFMs, such as $\text{Fe}_{1.3}\text{Sb}$ [29],

Mn_5Si_3 [30], Mn_3Ga [12], and Mn_3Sn [31–33]. In addition, the THE is also proposed for systems with skyrmion or nontrivial spin structures [34], and experimentally verified in frustrated magnets Fe_3Sn_2 [35], Gd_2PdSi_3 [36], and helimagnets MnSi [37], MnGe [38], etc. These properties deepen our understanding of the interplay between magnetism and electronic structure.

In two-dimensional materials, the transition metal dichalcogenide NbS_2 has attracted enormous interest. The layered structure allows the intercalation of magnetic atoms between the layers, which accompanies significant changes in physical properties [39,40]. Depending on the intercalant element, the materials $M_{1/3}\text{NbS}_2$ ($M = \text{V}, \text{Cr}, \text{Mn}, \text{Fe}, \text{Co}$) can be FMs such as $\text{Cr}_{1/3}\text{NbS}_2$ [41], $\text{Mn}_{1/3}\text{NbS}_2$ [42,43], or an AFM such as $\text{V}_{1/3}\text{NbS}_2$ [44–46] (it was proposed as nonmagnetic [47,48] or ferromagnetic material [39,49] in earlier studies), $\text{Fe}_{1/3}\text{NbS}_2$ [50–54], $\text{Co}_{1/3}\text{NbS}_2$ [20–22,55–57]. Owing to the competition between magnetic exchange interaction among the magnetic atoms and coupling between magnetic atoms and conduction electrons, abundant magnetic states have been observed in these materials, including the helimagnetic order, chiral magnetic soliton lattice, and other complex magnetic states [41]. Other properties, such as anisotropic magnetic interactions, giant magnetoresistance (MR), AHE, or THE, are usually observed. These findings establish the materials $M_{1/3}\text{NbS}_2$ ($M = \text{V}, \text{Cr}, \text{Mn}, \text{Fe}, \text{Co}$) as good candidates for hosting unique magnetic and transport

*tlxia@ruc.edu.cn

properties. Motivated by previous work, we investigate the magnetic properties and abundant magnetotransport properties of $V_{0.3}NbS_2$.

In this paper, we report the observation of the AHE, as well as THE and negative MR in the layered antiferromagnetic material $V_{0.3}NbS_2$. It orders antiferromagnetically below $T_{N1} \sim 53$ K and exhibits a weak hysteresis loop with tiny net magnetization (≈ 16 $m\mu_B/V$) along the c axis, which is brought by canted antiferromagnetic configuration. Despite the tiny net magnetization, prominent AHE is realized, which may result from the contribution of nonzero Berry curvature. THE is detected at low temperatures, which acts as the probe of spin reorientation in the magnetization process induced by field. The longitudinal resistivity shows a weak irreversible behavior around zero field, consistent with the hysteresis loop in magnetization and Hall resistivity. Negative MR is present below 7 T, which is ascribed to the spin-dependent scattering. $V_{0.3}NbS_2$ enriches the diversity of magnetic material systems, making itself a promising platform to realize various magnetotransport properties resulting from complex spin structures.

II. EXPERIMENT

Single crystals of $V_{0.3}NbS_2$ were grown by chemical vapor transport method with I_2 as the transport agent. The powders of V, Nb, and S with a ratio of 1:3:6 were sealed into a quartz tube. The tube was put into a furnace, which was heated to 900 °C and held for 5 days to prepare the polycrystalline precursor. Afterwards, the precursor powder (1 g) and 10 mg/cm³ of iodine were sealed into the quartz tube to grow single crystals. The end temperature of the quartz tube containing the materials was set as 950 °C (source) with the other end temperature as 800 °C (growth) and held for 10 days. Eventually, the single crystals with a shiny surface were obtained, which exhibited a hexagonal plate shape. The atomic composition was confirmed to be V:Nb:S = 0.3:1:2 by energy dispersive x-ray spectroscopy (EDS, Oxford X-Max 50). The slight deviation from $x \sim 0.33$ may come from the defects of magnetic atom V. The single-crystal x-ray diffraction (XRD) and powder XRD patterns were obtained on a Bruker D8 Advance x-ray diffractometer using Cu K_α radiation. TOPAS-4.2 was employed for the refinement. The measurements of resistivity and magnetic properties were performed on the Quantum Design physical property measurement system (QD PPMS-14 T) and Quantum Design magnetic property measurement system (QD MPMS-3).

The crystal structure of $V_{1/3}NbS_2$ with space group $P6_322$ (No. 182) is shown in Fig. 1(a), in which the intercalated magnetic atoms V occupy the sites between 2H-NbS₂ layers. Figure 1(b) shows the powder XRD patterns (powdered sample was obtained by crushing single crystals) and refinement result with space group $P6_322$ [45]. The obtained lattice parameters are $a = b = 5.760$ Å and $c = 12.153$ Å. The single crystal XRD pattern shown in Fig. 1(c) reveals the (001) crystalline surface. Inset displays a photograph of $V_{0.3}NbS_2$ single crystal with metallic luster. As displayed in Fig. 1(d), the temperature-dependent resistivity ρ_{yy} demonstrates the metallic behavior with a sudden drop at around 53 K, which originates from the electron scattering as the onset of spin ordering.

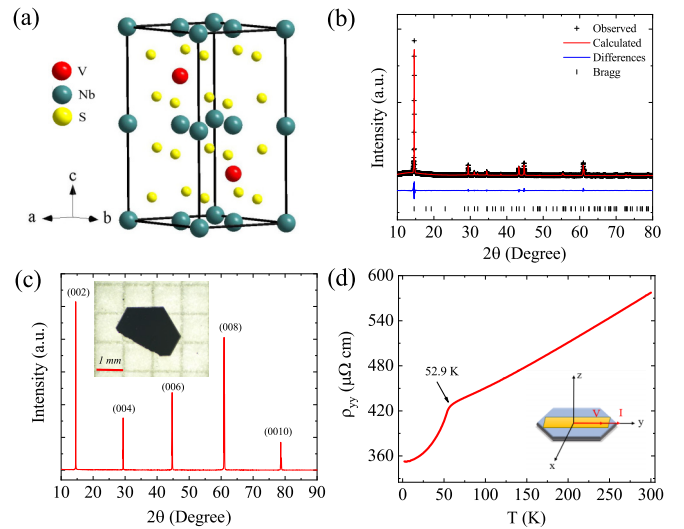


FIG. 1. (a) The crystal structure of $V_{1/3}NbS_2$ with space group $P6_322$ (No. 182). (b) Powder XRD pattern with refinement. $R_{wp} = 11.37\%$. (c) Single crystal XRD pattern of $V_{0.3}NbS_2$ with (001) surface. Inset shows the typical single crystal. (d) The temperature-dependent resistivity from 2 K to 300 K. Inset shows the measurement configuration.

III. MAGNETIZATION AND MAGNETIC RESPONSES

The temperature-dependent magnetic susceptibilities with $H//ab$ (χ^{ab}) and $H//c$ (χ^c) are conducted under $H=500$ Oe in zero-field-cooled (ZFC) and field-cooled (FC) modes, respectively. For both directions, magnetization curves nearly overlap at high temperature as shown in Fig. 2(a). A rapid

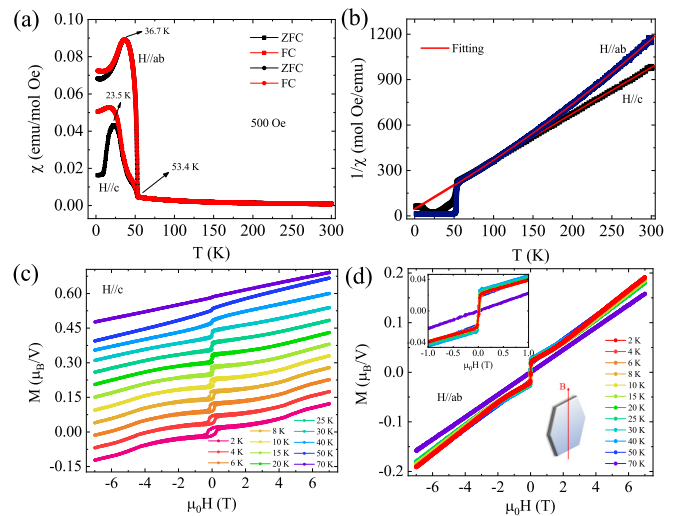


FIG. 2. (a) Temperature dependence of the magnetic susceptibilities along c axis and ab plane under 500 Oe, respectively. (b) The Curie-Weiss fits of inverse susceptibility along c axis and ab plane. (c) The magnetization of $V_{0.3}NbS_2$ with the field applied along c axis at different temperatures. The data except for 2 K is shifted upward for clear viewing. (d) The magnetization with the field along ab plane. Upper left inset shows the data around zero field. Bottom right inset shows the sketch map where the magnetic field lies in the ab plane and perpendicular to the hexagonal edge.

upturn is observed at 53 K, which indicates that the material orders magnetically at $T_{N1} \sim 53$ K. Below T_{N1} , χ^{ab} is larger than χ^c , denoting the easy magnetization along the ab plane, in agreement with reported work [39,44,45]. In addition, at $T_{N2}^{ab} \sim 36.7$ K for $H//ab$ and $T_{N2}^c \sim 23.5$ K for $H//c$, χ both decreases and bifurcates, corresponding to a second magnetic transition [39]. The values in different directions are not the same, which is probably due to the strong magnetic anisotropy [44]. The fits of ZFC data to modified Curie-Weiss law [58] $\chi = \chi_0 + C/(T - T_\theta)$ are displayed in Fig. 2(b), where χ_0 is the temperature-independent term resulting from the paramagnetism and diamagnetism. C stands for the Curie constant and T_θ represents the Weiss temperature. The fittings yield the effective moment $\mu_{\text{eff}}^{ab} = 3.04 \mu_B/V$ and $\mu_{\text{eff}}^c = 2.93 \mu_B/V$, close to the spin-only moment [39] of $2.83 \mu_B$ for V^{3+} . The negative Weiss temperatures $T_\theta^{ab} = -14.5$ K and $T_\theta^c = -15.2$ K indicate predominant antiferromagnetic interaction in paramagnetic state.

The field-dependent magnetizations $M(H)$ at various temperatures with $H//c$ and $H//ab$ are shown in Figs. 2(c) and 2(d), respectively. For both directions, the magnetizations are discovered to keep increasing as field increases and do not reach saturation up to 7 T. The maximum moment of $\sim 0.15 \mu_B/V$ with $H//c$ and $\sim 0.2 \mu_B/V$ with $H//ab$ are reached, substantially lower than the effective moment ($\mu_{\text{eff}}^{ab} = 3.04 \mu_B/V$ and $\mu_{\text{eff}}^c = 2.93 \mu_B/V$). These behaviors confirm the antiferromagnetic state in $V_{0.3}\text{NbS}_2$, consistent with the antiferromagnetic interaction from fittings shown in Fig. 2(b). A clear ferromagnetic hysteresis loop with a tiny net magnetization of $16 m\mu_B/V$ is observed at 2 K with $H//c$, which declines as the temperature increases and ultimately disappears near T_{N1} . Further, as field increases, magnetization with $H//c$ exhibits a nonlinear increasing behavior at low temperatures and tends to be linear around T_{N2}^c . In contrast, the hysteresis loop is absent with $H//ab$ and nonlinear increasing behavior is weakened when compared to the case along the c direction. The canted magnetic structure of $V_{0.3}\text{NbS}_2$ has been suggested by previous neutron diffraction [44,45], which results in the hysteresis loop and nonlinear increasing behavior. The magnetic moment of $V_{0.3}\text{NbS}_2$ involves two propagation vectors: \mathbf{k}_0 and \mathbf{k}_1 . The \mathbf{k}_0 is associated with an antiferromagnetic ordering along the a axis with a refined value of $0.90(5) \mu_B$, whereas \mathbf{k}_1 is associated with moments along the c axis in an up-down-down configuration with refined values of $1.21(12) \mu_B$ and $0.61(6) \mu_B$, respectively. The c -axis uncompensated spin components give rise to a net ferrimagnetic moment displayed in Fig. 2(c), and ab -plane compensated ones result in the antiferromagnetic state shown in Fig. 2(d). Combining the two propagation vectors, the down moment experiences a canting of 34° and the up moment is canted 55° out of the ab plane in the opposite direction [44]. The complex magnetic structures (see Appendix A) may generate more abundant spin configurations with field changing, probably being the origin of nonlinear increasing behavior.

IV. HALL EFFECT

Hall effect is one of the most fundamental physical property as an efficient method to explore the electrical properties of materials. Normal Hall effect, expressed as a function of

magnetic field H , is usually employed to reveal the dominant carrier types, carrier concentrations, and mobilities. However, in magnetic materials, there usually exists additional Hall signals characterized as AHE or THE, which are independent of applied magnetic field. Thus, the materials owning three Hall components can be expressed as

$$\rho_{yx} = \rho_{yx}^N + \rho_{yx}^A + \rho_{yx}^T. \quad (1)$$

One interesting feature in AFM $V_{0.3}\text{NbS}_2$ is simultaneous appearance of normal Hall ρ_{yx}^N , anomalous Hall ρ_{yx}^A , and topological Hall resistivity ρ_{yx}^T . Next, each component is discussed in detail.

A. Anomalous Hall effect

The component of normal Hall can be extracted by the linear fitting of $\rho_{yx} = \mu_0 R_0 H + b$ within high-field region (6 T–9 T), where R_0 is the normal Hall coefficient and b is the intercept. Meanwhile, ρ_{yx}^T occurs at low field and ρ_{yx}^A is present at zero field. Thus, the value of ρ_{yx}^A can be determined from the intercept b of linear fitting (see Appendix B). The field-dependent curve of $\rho_{yx}^A + \rho_{yx}^T$ is obtained by subtracting the normal Hall resistivity from the total resistivity. A typical example at 2 K showing the extraction is displayed in Fig. 3(b). The upper left inset shows the enlarged view near zero field. With the linear fitting between 6 T–9 T, the positive sign of R_0 demonstrates that the dominant carrier is hole type. The estimated carrier concentration n ($n = 1/|eR_0|$) and mobility μ ($\mu = 1/|en\rho_{yy}(0)|$) are obtained, and the temperature-dependent curves are displayed in the lower right inset of Fig. 3(b). Figure 3(c) denotes the temperature dependence of ρ_{yx}^A and calculated $\sigma_{yx}^A \sim -\rho_{yx}^A/\rho_{yy}^2$, both of which are nearly temperature independent below 30 K. This robust behavior against temperature indicates that the AHE phenomenon is not mainly governed by the scattering events. The combination of AHE and THE is shown in Fig. 3(d), in which evident THE is characterized as a hump at low field. Next, we discuss these two abnormal Hall effects, respectively.

In FMs, the anomalous Hall resistivity has a quantitative relation with magnetization M ,

$$\rho_{yx}^A = \mu_0 R_s M, \quad (2)$$

where μ_0 is the permeability of free space and R_s is the anomalous Hall coefficient. To examine the magnetization dependence of the AHE in $V_{0.3}\text{NbS}_2$, the anomalous Hall is plotted as a function of magnetization within the same field range (± 7 T). ρ_{yx}^A versus M at 30 K is shown in Fig. 3(e), which is prominent to be analyzed without THE. We note that ρ_{yx}^A exhibits a hysteresis loop at low field (see data at 2 K in Appendix C), similar to the behavior seen in Mn_3Sn [14], Mn_3Ge [59], and CoNb_3S_6 [20]. To emphasize, the magnetization-independent ρ_{yx}^A behavior is demonstrated, indicating that the Eq. (2) applied to FM materials is invalid for AFM $V_{0.3}\text{NbS}_2$. In addition, as a method usually adopted to analyze the AHE in FM materials, the relation $\rho_{yx}^A \propto \rho_{yy}^\alpha$ is employed to judge on the mechanism beneath. For skew scattering, $\alpha = 1$, while for side-jump scattering or intrinsic nonzero Berry-curvature ones, $\alpha = 2$. The parameter α can be obtained through linear fitting of $\log_{10} \rho_{yx}^A$ versus $\alpha \log_{10} \rho_{yy}$.

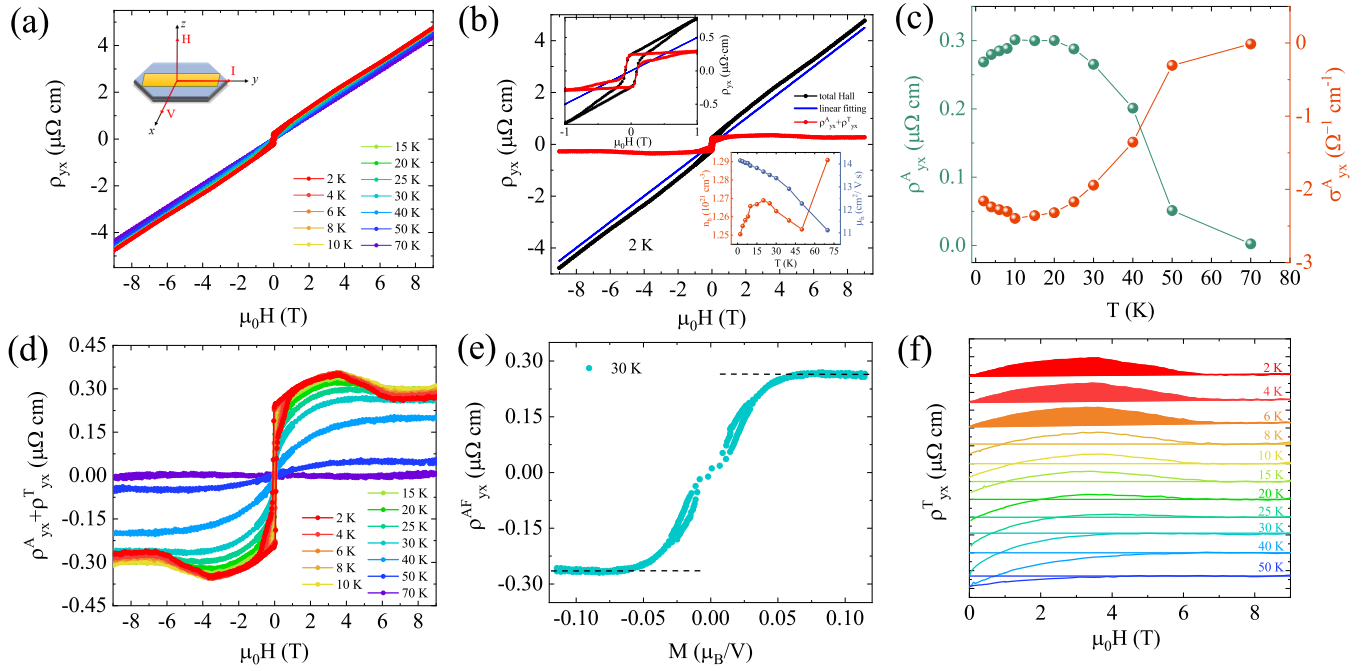


FIG. 3. (a) The field dependence of Hall resistivities with $H//c$ axis at different temperatures. Inset shows the geometric sketch of measurement. (b) The raw data, the linear fitting, and $\rho_{yx}^A + \rho_{yx}^T$ after subtracting normal Hall resistivity at 2 K. Upper left inset: Enlarged view around zero field. Lower right inset: The temperature dependence of carrier concentration and mobility. (c) The temperature-dependent anomalous Hall resistivity ρ_{yx}^A and anomalous Hall conductivity σ_{yx}^A . (d) The $\rho_{yx}^A + \rho_{yx}^T$ after subtracting normal Hall resistivity at various temperatures. (e) Magnetization-dependent ρ_{yx}^{AF} at 30 K. (f) The field-dependent topological Hall resistivities at various temperatures. The data is shifted downward for clarity.

However, the relation breaks down in $V_{0.3}\text{NbS}_2$, as displayed in Appendix D, where the linear behavior of $\log_{10} \rho_{yx}^A(T)$ versus $\log_{10} \rho_{yy}(T)$ is not satisfied. Therefore, the weak c -axis ferromagnetic component is not the origin of AHE in $V_{0.3}\text{NbS}_2$. In other words, there exists another dominant contribution to AHE, labeled ρ_{yx}^{AF} , which is independent of H or M and driven by the antiferromagnetic order. Accordingly, Eq. (1) is rewritten as

$$\rho_{yx} = \rho_{yx}^N + \rho_{yx}^{AF} + \rho_{yx}^T \quad (3)$$

Normally, for FMs, coefficients $R_s = \rho_{yx}^A / \mu_0 M_s$ or $S_H = \sigma_{xy}^A / \mu_0 M_s \sim R_s / \rho_{yy}^2$ are employed to estimate the strength or amplitude of AHE, where M_s is the saturation of magnetization in FMs [60]. Although ρ_{yx}^{AF} demonstrates a M -independent behavior as shown in Fig. 3(e), the same method is employed and $R_s^0 = \rho_{yx}^{AF} / \mu_0 M(H=0)$ is defined as the spontaneous component at zero field to evaluate the AHE in $V_{0.3}\text{NbS}_2$. It is $643.1 \mu\Omega \text{ cm}/T$ at 2 K, three orders larger than normal Hall coefficient $R_0 \sim 0.50 \mu\Omega \text{ cm}/T$. It is also meaningful to estimate the value of $S_H^0 = \sigma_{xy}^{AF} / \mu_0 M(H=0) \sim R_s^0 / \rho_{yy}^2(H=0)$. It reaches 0.65 V^{-1} at 2 K, even larger than the values in FMs, such as Fe (0.06 V^{-1}) [61], Ni (-0.14 V^{-1}) [62], MnSi (-0.19 V^{-1}) [63], Co_2CrAl (0.039 V^{-1}) [64]. These significantly large coefficients of AHE mainly come from small magnetization at zero field. The discussions above indicate that ρ_{yx}^{AF} in $V_{0.3}\text{NbS}_2$ cannot be defined by the criterion of AHE in FMs. It may come from the contribution of nonzero Berry curvature.

The large AHE is predicted in noncollinear or noncoplanar AFMs [10,11] and observed in Mn_3X ($X = \text{Ga, Ge, Sn, Ir, Pt}$) [12–17], Mn_5Si_3 [18,19], and $\text{Co}_{1/3}\text{NbS}_2$ [20–22], or materials with complex spin structure, such as $\text{Pr}_2\text{Ir}_2\text{O}_7$ [23] and $\text{Nd}_2\text{Mo}_2\text{O}_7$ [24]. In these materials, the AHE is regarded as the result of nonzero Berry curvature. As the precondition to induce Berry curvature, the breaking of time-reversal symmetry or effective time-reversal symmetry $R_s T$ in which R_s is the rotation symmetry, etc. [65] is necessary [10,11]. Meanwhile, the role of SOC is also discussed. The SOC is necessary to break effective time-reversal symmetry in coplanar (noncollinear) AFMs, resulting in nonzero Berry curvature. However, noncoplanar spin system breaks $R_s T$ as well as T , leading to the nonzero Berry curvature even without considering SOC. $V_{0.3}\text{NbS}_2$ is reported as an AFM with noncollinear spin configuration [44,45], whereas it can be regarded as noncoplanar when Honeycomb-type lattice is considered as a unit (see Appendix A). Hence, further theoretical calculations are desired to judge the type of spin configuration that induces the AHE in $V_{0.3}\text{NbS}_2$, which mainly depends on the analysis of symmetries. Extrinsic mechanisms involving skew scattering or side jump are strongly related to SOC and depends on the magnetization M [5], which may not apply to the AHE in AFMs. Other mechanisms about AHE in AFMs, except for the contribution of Berry curvature, are still unclear. Further theories are in great demand to uncover the physics beneath. As discussed above, based on the noncollinear/noncoplanar antiferromagnetic spin configuration, related calculations and analyses are of great importance to verify the mechanism of AHE in $V_{0.3}\text{NbS}_2$. The topo-

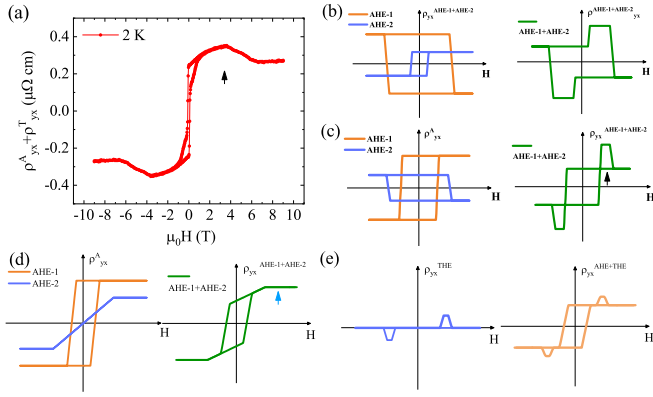


FIG. 4. (a) The $\rho_{yx}^A + \rho_{yx}^T$ after subtracting normal Hall resistivity at 2 K. Different illustrations showing how the peaks arise due to (b)–(d) the two-channel AHE or (e) AHE+THE.

logically nontrivial band structure is expected to be realized in $V_{0.3}NbS_2$, promoting the studies of AHE in AFMs and extending its great potential for spintronic devices further.

B. Topological Hall effect

To analyze the THE in $V_{0.3}NbS_2$, ρ_{yx}^T is extracted by subtracting the anomalous Hall resistivity from data, as shown in Fig. 3(f). At 2 K, ρ_{yx}^T reaches a maximum value of about $0.1 \mu\Omega \text{ cm}$ at $\sim 4 \text{ T}$. Its magnitude decreases when temperature increases, and ultimately disappears above 25 K, around the temperature T_{N2}^C . Synchronously, the hump shifts to higher field and the region gradually narrows.

Recent work indicates that the combination of two AHE hysteresis loops gives rise to a peak signal that looks like a THE, which is called the two-channel AHE model [66]. In this paper, the data is carefully analyzed and the possibility of such a mechanism is ruled out.

First, the two-channel AHE model is generally observed in films or heterostructures, which is considered to originate from the thickness variation, defects, or interface modifications. However, such effects are negligible in bulk materials. Second, we assume that the Hall curve as shown in Fig. 4(a) is wrongly interpreted as the sum of AHE and THE, which should be interpreted as two-channel AHE model. We try to resolve the possible shape of the two AHE curves, as depicted in Figs. 4(b)–4(d), in which the orange and blue lines represent two individual AHE curves and the green one is the sum. In fact, Figs. 4(b) and 4(c) were proposed in a recent study [66], in which both AHE curves own hysteresis loops. Considering the characteristic of the AHE curve in $V_{0.3}NbS_2$, we further propose another possibility in Fig. 4(d), where one AHE curve owns the loop while the other does not. Thus, all types of AHE curves and the sum of them are considered. Three typical cases are presented in Figs. 4(b)–4(d) as others are equivalent or deviate significantly from the experimental curves in Fig. 4(a).

Next, all the possibilities of two-channel AHE models are discussed and ruled out one by one. The possibility as shown in Fig. 4(b) is excluded since the AHE show both positive and negative values at positive/negative field which is different from the AHE curve in $V_{0.3}NbS_2$ [Fig. 4(a)]. The possibility

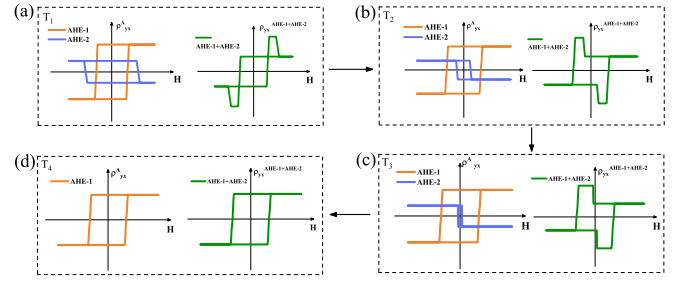


FIG. 5. The evolution of two-channel AHE model with temperature increasing ($T_4 > T_3 > T_2 > T_1$).

shown in Fig. 4(c) is excluded because the closed peak does not match the situation with the almost overlapped curves in $V_{0.3}NbS_2$ [Fig. 4(a)], which is marked with black arrows. The possibility shown in Fig. 4(d) is also excluded because only a gradient curve instead of a peak is formed after adding two AHE curves together, which is marked with the blue arrow in Fig. 4(d). Thus, only the AHE+THE interpretation shown in Fig. 4(e) is consistent with the curve in $V_{0.3}NbS_2$ [Fig. 4(a)]. It is worth noting that the curves of THE are coincident with sweeping the field forward and backward, as shown in Fig. 4(e), which is commonly observed in previous reports [12,67,68]. The other possible type of THE is discussed in Ref. [66], which does not coincide in back-and-forth field sweeping modes and is different from our results.

Third, if the peak signal on Hall curves formed by the sum of two-channel AHE only arises over a small temperature range below T_C/T_N , it indicates that these two AHE present different temperature dependencies [69]. For example, the value and loop of AHE-2 gradually decrease as the temperature increases from T_1 to T_3 , and then disappears at T_4 , as shown in Figs. 5(a)–5(d) (in this warming process, for simplicity, we assume that the AHE-1 remains unchanged and only AHE-2 changes to analyze the effect of AHE-2 on the final curves). The shape of the final curve AHE-1+AHE-2 does change as expected, as illustrated in Fig. 5. The situation becomes more complicated when the sign of AHE-1 or AHE-2 changes, as reported in $SrRuO_3$ film [69]. In our experimental results on $V_{0.3}NbS_2$, the peak signal on the Hall curve only exists below 30 K ($T_N \sim 53 \text{ K}$). However, different from the two-channel AHE model, the shape of the final curve as well as the sign of AHE and THE remains similar over the whole temperature region (up to about 70 K). The variation of the peak signal with the temperature and the field is in accordance with the law of THE.

Based on above discussions, we preclude the possibility that the peak signal on Hall curve originates from the combination of two AHE channels and confirm that it is indeed contributed by the THE. Essentially, the THE is the result of effective magnetic flux generated by electrons passing through a spin texture, which is also defined as a Hall effect resulting from a real-space Berry curvature [28]. Previously, the THE was extensively studied in FMs owning spin textures with nonzero chirality, including skyrmions, chiral domain walls, or magnetic frustrations [28], which was ascribed to the topology of spin textures as reported previously [25,26,28,34]. Thus, the THE in AFMs is considered to be nonexistent

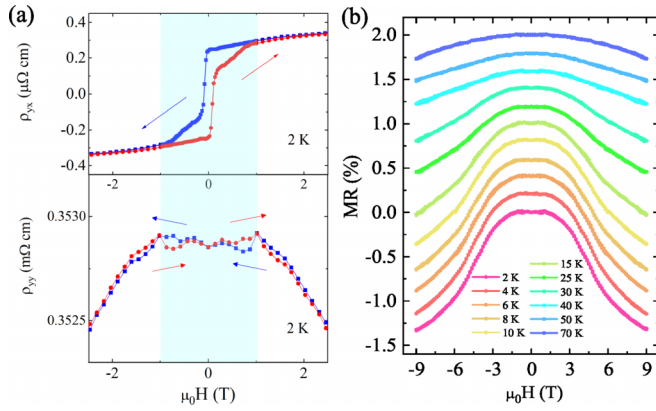


FIG. 6. (a) The Hall resistivity and longitudinal resistivity as a function of magnetic field at 2 K. (b) The field dependence of MR with $H//c$ at different temperatures.

due to the cancellation of spin chirality. However, the THE are expected in canted AFMs in theories [27,70]. In fact, in Mn_3Sn with a noncollinear antiferromagnetic ground state, a large THE is observed by the application of field to induce noncoplanar antiferromagnetic geometry [31]. Similar experimental observations were also reported in other materials [12,30,32,33]. In $\text{V}_{0.3}\text{NbS}_2$, as the field is applied along the c axis and increases, spins tend to be aligned towards the c axis and spin reorientation is formed in the magnetization process, exhibited by nonlinear behavior below T_{N2}^c in magnetization curve as shown in Fig. 2(c). In this process, spin texture is generated (see Appendix A). As the temperature increases, the fluctuation suppresses spin reorientation, and the nonlinear behavior as well as THE disappear above T_{N2}^c . Both the temperature dependence and field dependence of THE in $\text{V}_{0.3}\text{NbS}_2$ indicate its possible origin from the different field-induced spin textures. The possible existence of other complex mechanisms, such as nontrivial spin textures, chiral helimagnets, or skyrmions, needs further study.

V. MAGNETORESISTIVITY

Magnetoresistance measurements were performed to study the transport response induced by the field. The field-dependent Hall and longitudinal resistivity with $H//c$ are shown in Fig. 6(a). Within the ± 1 T region marked with cyan shadow, ρ_{yy} exhibits a plateau with irreversible behavior, consistent with the hysteresis loop on Hall resistivity and magnetization. As the field increases, negative MR is detected as shown in Fig. 6(b). The result originates from the spin-dependent scattering, which can be explained by the two-current model in magnetic materials [58]. Spins in AFMs are antiparallel aligned at zero field and the scattering occurs both in two spin channels (spin-up and spin-down conducting electrons), corresponding to the high-resistance state. An applied field, progressively aligning the magnetization, opens the conducting channel between the same spins, corresponding to the low-resistance state. Thus, the scattering between conducting electrons and magnetic moments with different spin directions is suppressed, leading to the negative MR [71–76]. With further increasing field, the decreasing trend

of negative MR in $\text{V}_{0.3}\text{NbS}_2$ slows down, resulting from the increase of positive orbital MR. From the magnetotransport study, the effect of magnetic order on transport properties in $\text{V}_{0.3}\text{NbS}_2$ is revealed, providing an ideal platform to study the anomalous transport in AFM.

VI. SUMMARY

Recently, noncollinear/noncoplanar magnetic materials have attracted a great deal of attention due to their highly tunable magnetic states and great potential on spintronic devices. $\text{V}_{0.3}\text{NbS}_2$, as a noncollinear AFM, presents abundant magnetic and magnetotransport properties. It orders antiferromagnetically at $T_{N1} \sim 53$ K, below which it shows a magnetic hysteresis loop with tiny net magnetization ($\approx 16 m\mu_B/V$) along the c axis, as a result of canted antiferromagnetic configuration. Prominent AHE is realized in AFM with nearly perfect cancellation of moments, indicating the possible existence of nonzero Berry curvature. The observation of THE in $\text{V}_{0.3}\text{NbS}_2$ captures the spin-reorientation in the magnetization process induced by field. MR shows a weak irreversible behavior around zero field, corresponding to the hysteresis loop in magnetization and Hall resistivity. It presents negative value below 7 T, resulting from the spin-dependent scattering.

ACKNOWLEDGMENTS

This work is supported by the National Key R & D Program of China (No. 2019YFA0308602), the National Natural Science Foundation of China (Grants No. 12074425 and No. 11874422), and the Fundamental Research Funds for the Central Universities, and the Research Funds of Renmin University of China (Grants No. 18XNLG14 and No. 19XNLG18). H.W. is also supported by the Outstanding Innovative Talents Cultivation Funded Programs 2020 of Renmin University of China.

APPENDIX A: SCHEMATIC ILLUSTRATION OF THE SPIN CONFIGURATION IN $\text{V}_{0.3}\text{NbS}_2$.

$\text{V}_{0.3}\text{NbS}_2$ is reported as a noncollinear AFM with spins lying on the ac plane [44]. The magnetic moments of the vanadium atoms on each layer are displayed in Fig. 7(b). When considering the vanadium atoms in the adjacent unit cells and layers, a honeycomb-type configuration is formed as shown in Figs. 7(a) and 7(c). This kind of analysis is commonly employed in magnetic materials [10,59,77] when considering the magnetic interactions between atoms located at different sites. Taking the honeycomb-type configuration as a unit, all spins are now noncoplanar as shown in Fig. 7(c) when the field is applied along the c axis to measure the Hall resistivity. Therefore, further theoretical calculations are desired to judge the type of spin configuration that induces the AHE in $\text{V}_{0.3}\text{NbS}_2$, which mainly depends on the analysis of symmetries. Moreover, complex magnetic structures are possibly formed as field is applied along the c axis and increases, which result in the THE in $\text{V}_{0.3}\text{NbS}_2$.

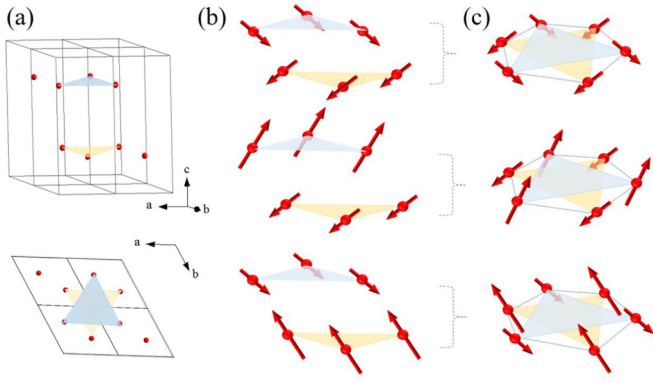


FIG. 7. (a) The vanadium atoms in $2 \times 2 \times 1$ unit cells of $V_{0.3}NbS_2$ along different directions. (b) Magnetic moments of the vanadium atoms on each layers of $V_{0.3}NbS_2$. The arrow represents V magnetic moment. (c) Schematic illustration with the magnetic moments of the vanadium atoms in the unit of honeycomb lattice.

APPENDIX B: THE ANOMALOUS HALL RESISTIVITY OBTAINED WITH TWO METHODS

There exist two common types of anomalous Hall curves in FMs, one with a hysteresis loop and the other without, as shown in Figs. 8(a) and 8(b), which in general coincides with the magnetization curve, corresponding to the hard and soft magnets, respectively. For ρ_{yx} curves with hysteresis loop, the value at zero field is directly read as the anomalous Hall resistivity, which has the same value with that at high field. For ρ_{yx} curves without hysteresis loop, the saturation curve at high field is extended to zero field, namely, the intercept of linear fitting of normal Hall resistivity, and the anomalous Hall resistivity is obtained. Actually, these two methods are essentially the same for FMs, which were employed in previous reports [78,79], indicating that the anomalous Hall resistivity ρ_{yx}^A is field independent. The presence/absence of the hysteresis loop is just the transport response of hard or soft magnets, rather than the necessary condition to judge the existence of AHE. The anomalous Hall resistivity should be the value after subtraction of the normal Hall resistivity at high field. The same analytical procedure can be applied to AFMs. In general, the hysteresis loop on magnetization may originate from the presence of ferromagnetic component,

and the hysteresis loop on Hall or longitudinal resistivity is the consequence in transport responses. These two methods are both employed to obtain the anomalous Hall resistivity in $V_{0.3}NbS_2$, as shown in Fig. 8(c), which exhibits a large difference. More importantly, as analyzed in the main text, the tiny net magnetization due to uncompensated spin moment along the c axis is not the origin of AHE in $V_{0.3}NbS_2$. In conclusion, the resistivities read at zero field are viewed as a transport response of the uncompensated spin moment along the c axis, while the values obtained from linear fittings are viewed as the anomalous Hall resistivities in $V_{0.3}NbS_2$.

APPENDIX C: THE ANOMALOUS AND TOPOLOGICAL HALL RESISTIVITY AT 2 K AFTER SUBTRACTING NORMAL HALL RESISTIVITY

The combination of anomalous Hall and topological Hall resistivity is obtained by subtracting the normal Hall component from total Hall resistivity. The field-dependent curve is displayed in Fig. 9(a). To examine the magnetization dependence, $\rho_{yx}^A + \rho_{yx}^T$ versus magnetization is plotted in Fig. 9(b). It shows a prominent hysteresis loop at low field, the same as the behavior observed in Mn_3Sn [14], Mn_3Ge [59], and $CoNb_3S_6$ [20], indicating that ρ_{yx} has an additional spontaneous term ρ_{yx}^{AF} independent of M as described by Eq. (3) in the main text. In the low-field regime, the topological Hall resistivity exists and the curve is difficult to be analyzed. Thus, the data at 30 K without topological Hall is displayed as an example in the main text.

APPENDIX D: THE ANALYSIS OF AHE CRITERIA

Normally, in ferromagnetic materials, the relation $\rho_{yx}^A \propto \rho_{yy}^\alpha$ (ρ_{yy} is the longitudinal resistivity at zero field) is employed as the criterion to reveal the mechanism of AHE. α equals 1 for skew-scattering, while α equals 2 for intrinsic nonzero Berry-curvature and side-jump scattering. The parameter α can be obtained through linear fitting of $\log_{10} \rho_{yx}^A$ versus $\alpha \log_{10} \rho_{yy}$. However, as shown in Fig. 10(a), the non-linear behavior is observed between $\log_{10} \rho_{yx}^{AF}$ and $\log_{10} \rho_{yy}$ in $V_{0.3}NbS_2$. Further, the scaling relation between conductivities for the extrinsic mechanism ($\sigma_{xy}^A \propto \sigma_{yy}^{1.6}$ or $\sigma_{xy}^A \propto \sigma_{yy}$) and intrinsic mechanism ($\sigma_{xy}^A \propto \text{const}$) has also been proposed as a criterion previously [15]. As shown in Fig. 10(b), the

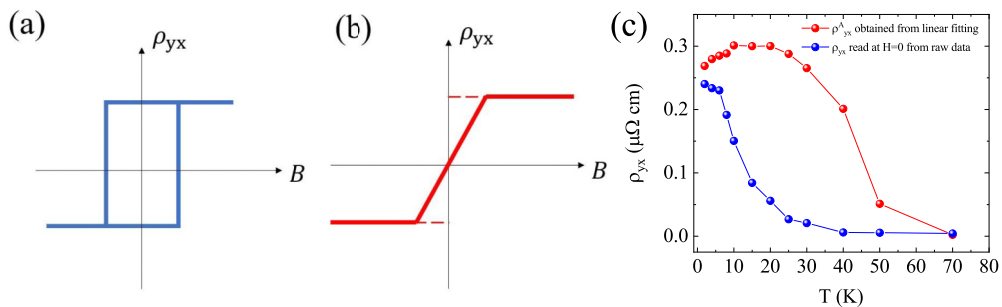


FIG. 8. Two types of Hall resistivity curve in magnets, one (a) with hysteresis loop and the other (b) without. (c) The temperature dependence of anomalous Hall resistivity obtained from linear fitting (plotted with red balls) and Hall resistivity read at zero field from raw data (plotted with blue balls).

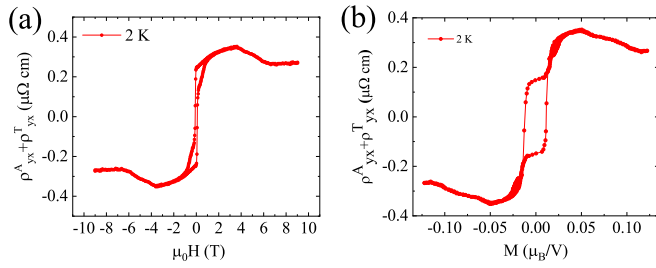


FIG. 9. (a) The field and (b) magnetization dependence of $\rho_{yx}^A + \rho_{yx}^T$ at 2 K.

criterion does not apply in $V_{0.3}\text{NbS}_2$ either. In addition, the Hall resistivity read at zero field from raw data as discussed in Sec. II is also examined with the same methods. Similarly, a nonlinear behavior between $\log_{10} \rho_{yx}$ and $\log_{10} \rho_{yy}$ is shown in Fig. 10(c). Although linear behavior between $\log_{10} \sigma_{xy}$ and $\log_{10} \sigma_{yy}$ is demonstrated in Fig. 10(d), parameter 0.13 does not agree with the values of criterion. This analysis suggests that AHE in $V_{0.3}\text{NbS}_2$ cannot be explained with the criteria applied in FMs. Based on current theories [10,11], the contribution of nonzero Berry curvature is expected in $V_{0.3}\text{NbS}_2$.

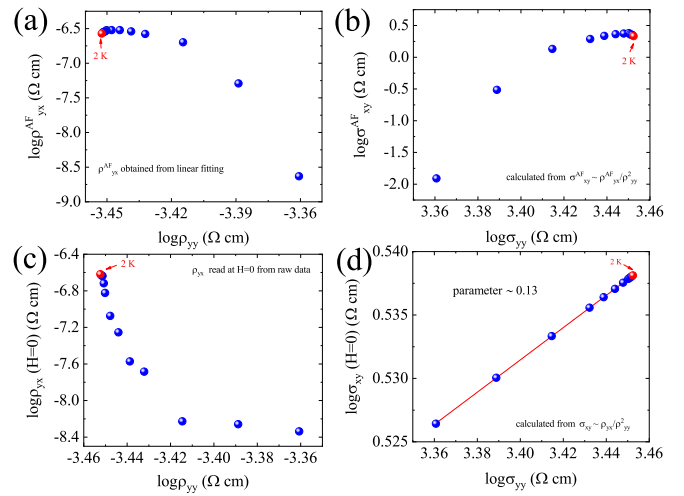


FIG. 10. The fitting of anomalous Hall resistivity ρ_{yx}^A [(a) obtained by linear fitting and (c) obtained by raw data] versus longitudinal resistivity ρ_{yy} . The fitting of anomalous Hall conductivity σ_{yx}^A [(b) calculated by ρ_{yx}^A from linear fitting (d) calculated by ρ_{yx}^A from raw data] versus longitudinal conductivity σ_{yy} .

- [1] E. Hall, *London Edinburgh Philos. Mag. J. Sci.* **10**, 301 (1880).
- [2] E. Hall, *London Edinburgh Philos. Mag. J. Sci.* **12**, 157 (1881).
- [3] R. Karplus and J. M. Luttinger, *Phys. Rev.* **95**, 1154 (1954).
- [4] T. Jungwirth, Q. Niu, and A. H. MacDonald, *Phys. Rev. Lett.* **88**, 207208 (2002).
- [5] N. Nagaosa, J. Sinova, S. Onoda, A. H. MacDonald, and N. P. Ong, *Rev. Mod. Phys.* **82**, 1539 (2010).
- [6] L. Šmejkal, A. H. MacDonald, J. Sinova, S. Nakatsuji, and T. Jungwirth, *Nat. Rev. Mater.* **7**, 482 (2022).
- [7] V. Bonbien, F. Zhuo, A. Salimath, O. Ly, A. About, and A. Manchon, *J. Phys. D: Appl. Phys.* **55**, 103002 (2022).
- [8] R. Shindou and N. Nagaosa, *Phys. Rev. Lett.* **87**, 116801 (2001).
- [9] J. Kübler and C. Felser, *Europhys. Lett.* **108**, 67001 (2014).
- [10] H. Chen, Q. Niu, and A. H. MacDonald, *Phys. Rev. Lett.* **112**, 017205 (2014).
- [11] M.-T. Suzuki, T. Koretsune, M. Ochi, and R. Arita, *Phys. Rev. B* **95**, 094406 (2017).
- [12] Z. Liu, Y. Zhang, G. Liu, B. Ding, E. Liu, H. M. Jafri, Z. Hou, W. Wang, X. Ma, and G. Wu, *Sci. Rep.* **7**, 515 (2017).
- [13] A. K. Nayak, J. E. Fischer, Y. Sun, B. Yan, J. Karel, A. C. Komarek, C. Shekhar, N. Kumar, W. Schnelle, J. Kübler *et al.*, *Sci. Adv.* **2**, e1501870 (2016).
- [14] S. Nakatsuji, N. Kiyohara, and T. Higo, *Nature* **527**, 212 (2015).
- [15] T. Chen, T. Tomita, S. Minami, M. Fu, T. Koretsune, M. Kitatani, I. Muhammad, D. Nishio-Hamane, R. Ishii, F. Ishii *et al.*, *Nat. Commun.* **12**, 1 (2021).
- [16] J. M. Taylor, E. Lesne, A. Markou, F. K. Dejene, P. K. Sivakumar, S. Pöllath, K. G. Rana, N. Kumar, C. Luo, H. Ryll *et al.*, *Appl. Phys. Lett.* **115**, 062403 (2019).
- [17] J. Mukherjee, T. S. Suraj, H. Basumatary, K. Sethupathi, and K. V. Raman, *Phys. Rev. Mater.* **5**, 014201 (2021).
- [18] C. Sürgers, T. Wolf, P. Adelman, W. Kittler, G. Fischer, and H. v. Löhneysen, *Sci. Rep.* **7**, 1 (2017).
- [19] C. Sürgers, W. Kittler, T. Wolf, and H. v. Löhneysen, *AIP Adv.* **6**, 055604 (2016).
- [20] N. J. Ghimire, A. Botana, J. Jiang, J. Zhang, Y.-S. Chen, and J. Mitchell, *Nat. Commun.* **9**, 3280 (2018).
- [21] G. Tenasini, E. Martino, N. Ubrig, N. J. Ghimire, H. Berger, O. Zaharko, F. Wu, J. F. Mitchell, I. Martin, L. Forró, and A. F. Morpurgo, *Phys. Rev. Res.* **2**, 023051 (2020).
- [22] S. Mangelsen, P. Zimmer, C. Näther, S. Mankovsky, S. Polesya, H. Ebert, and W. Bensch, *Phys. Rev. B* **103**, 184408 (2021).
- [23] Y. Machida, S. Nakatsuji, S. Onoda, T. Tayama, and T. Sakakibara, *Nature* **463**, 210 (2010).
- [24] Y. Taguchi, Y. Oohara, H. Yoshizawa, N. Nagaosa, and Y. Tokura, *Science* **291**, 2573 (2001).
- [25] J. Ye, Y. B. Kim, A. J. Millis, B. I. Shraiman, P. Majumdar, and Z. Tešanović, *Phys. Rev. Lett.* **83**, 3737 (1999).
- [26] P. Bruno, V. K. Dugaev, and M. Taillefumier, *Phys. Rev. Lett.* **93**, 096806 (2004).
- [27] J. J. Nakane, K. Nakazawa, and H. Kohno, *Phys. Rev. B* **101**, 174432 (2020).
- [28] H. Wang, Y. Dai, G. M. Chow, and J. Chen, *Prog. Mater. Sci.* **130**, 100971 (2022).
- [29] Y. Shiomi, M. Mochizuki, Y. Kaneko, and Y. Tokura, *Phys. Rev. Lett.* **108**, 056601 (2012).
- [30] C. Sürgers, G. Fischer, P. Winkel, and H. v. Löhneysen, *Nat. Commun.* **5**, 3400 (2014).
- [31] P. K. Rout, P. V. Prakash Madduri, S. K. Manna, and A. K. Nayak, *Phys. Rev. B* **99**, 094430 (2019).
- [32] J. Yan, X. Luo, H. Lv, Y. Sun, P. Tong, W. Lu, X. Zhu, W. Song, and Y. Sun, *Appl. Phys. Lett.* **115**, 102404 (2019).
- [33] J. M. Taylor, A. Markou, E. Lesne, P. K. Sivakumar, C. Luo, F. Radu, P. Werner, C. Felser, and S. S. P. Parkin, *Phys. Rev. B* **101**, 094404 (2020).

- [34] M. Onoda, G. Tatara, and N. Nagaosa, *J. Phys. Soc. Jpn.* **73**, 2624 (2004).
- [35] H. Li, B. Ding, J. Chen, Z. Li, Z. Hou, E. Liu, H. Zhang, X. Xi, G. Wu, and W. Wang, *Appl. Phys. Lett.* **114**, 192408 (2019).
- [36] T. Kurumaji, T. Nakajima, M. Hirschberger, A. Kikkawa, Y. Yamasaki, H. Sagayama, H. Nakao, Y. Taguchi, T.-h. Arima, and Y. Tokura, *Science* **365**, 914 (2019).
- [37] A. Neubauer, C. Pfleiderer, B. Binz, A. Rosch, R. Ritz, P. G. Niklowitz, and P. Böni, *Phys. Rev. Lett.* **102**, 186602 (2009).
- [38] N. Kanazawa, Y. Onose, T. Arima, D. Okuyama, K. Ohoyama, S. Wakimoto, K. Kakurai, S. Ishiwata, and Y. Tokura, *Phys. Rev. Lett.* **106**, 156603 (2011).
- [39] S. Parkin and R. Friend, *Philos. Mag. B* **41**, 65 (1980).
- [40] S. Parkin and R. Friend, *Philos. Mag. B* **41**, 95 (1980).
- [41] Y. Cao, Z. Huang, Y. Yin, H. Xie, B. Liu, W. Wang, C. Zhu, D. Mandrus, L. Wang, and W. Huang, *Mater. Today Adv.* **7**, 100080 (2020).
- [42] S. K. Karna, F. N. Womack, R. Chapai, D. P. Young, M. Marshall, W. Xie, D. Graf, Y. Wu, H. Cao, L. DeBeer-Schmitt, P. W. Adams, R. Jin, and J. F. DiTusa, *Phys. Rev. B* **100**, 184413 (2019).
- [43] Y. Dai, W. Liu, Y. Wang, J. Fan, L. Pi, L. Zhang, and Y. Zhang, *J. Phys.: Condens. Matter* **31**, 195803 (2019).
- [44] A. E. Hall, D. D. Khalyavin, P. Manuel, D. A. Mayoh, F. Orlandi, O. A. Petrenko, M. R. Lees, and G. Balakrishnan, *Phys. Rev. B* **103**, 174431 (2021).
- [45] K. Lu, D. Sapkota, L. DeBeer-Schmitt, Y. Wu, H. B. Cao, N. Mannella, D. Mandrus, A. A. Aczel, and G. J. MacDougall, *Phys. Rev. Mater.* **4**, 054416 (2020).
- [46] B. Sharma, R. Sharma, S. Kour, M. D. Sharma, O. Amin, A. R. Maity, and R. Mukherjee, *Indian J. Phys.* **96**, 1335 (2022).
- [47] F. Hulliger and E. Pobitschka, *J. Solid State Chem.* **1**, 117 (1970).
- [48] M. Nakanishi, Y. Matsuno, T. Fujii, J. Takada, and K. Yoshimura, *J. Phys. Chem. Solids* **69**, 49 (2008).
- [49] T. Inoshita, M. Hirayama, N. Hamada, H. Hosono, and S. Murakami, *Phys. Rev. B* **100**, 121112 (2019).
- [50] S. C. Haley, S. F. Weber, T. Cookmeyer, D. E. Parker, E. Maniv, N. Maksimovic, C. John, S. Doyle, A. Maniv, S. K. Ramakrishna *et al.*, *Phys. Rev. Res.* **2**, 043020(R) (2020).
- [51] S. F. Weber and J. B. Neaton, *Phys. Rev. B* **103**, 214439 (2021).
- [52] N. L. Nair, E. Maniv, C. John, S. Doyle, J. Orenstein, and J. G. Analytis, *Nat. Mater.* **19**, 153 (2020).
- [53] S. Wu, Z. Xu, S. C. Haley, S. F. Weber, A. Acharya, E. Maniv, Y. Qiu, A. A. Aczel, N. S. Settineri, J. B. Neaton, J. G. Analytis, and R. J. Birgeneau, *Phys. Rev. X* **12**, 021003 (2022).
- [54] E. Maniv, N. L. Nair, S. C. Haley, S. Doyle, C. John, S. Cabrini, A. Maniv, S. K. Ramakrishna, Y.-L. Tang, P. Ercius *et al.*, *Sci. Adv.* **7**, eabd8452 (2021).
- [55] H. Park, O. Heinonen, and I. Martin, *Phys. Rev. Mater.* **6**, 024201 (2022).
- [56] X. P. Yang, H. LaBollita, Z.-J. Cheng, H. Bhandari, T. A. Cochran, J.-X. Yin, M. S. Hossain, I. Belopolski, Q. Zhang, Y. Jiang *et al.*, *Phys. Rev. B* **105**, L121107 (2022).
- [57] H. Tanaka, S. Okazaki, K. Kuroda, R. Noguchi, Y. Arai, S. Minami, S. Ideta, K. Tanaka, D. Lu, M. Hashimoto *et al.*, *Phys. Rev. B* **105**, L121102 (2022).
- [58] S. Blundell, *Magnetism in Condensed Matter*, Oxford Master Series (Oxford University Press, Oxford, 2001).
- [59] N. Kiyohara, T. Tomita, and S. Nakatsuji, *Phys. Rev. Appl.* **5**, 064009 (2016).
- [60] Q. Wang, S. Sun, X. Zhang, F. Pang, and H. Lei, *Phys. Rev. B* **94**, 075135 (2016).
- [61] P. N. Dheer, *Phys. Rev.* **156**, 637 (1967).
- [62] J.-P. Jan and H. Gijssman, *Physica* **18**, 339 (1952).
- [63] A. Neubauer, C. Pfleiderer, R. Ritz, P. Niklowitz, and P. Böni, *Phys. B: Condens. Matter* **404**, 3163 (2009).
- [64] A. Husmann and L. J. Singh, *Phys. Rev. B* **73**, 172417 (2006).
- [65] R, T is taken as effective time-reversal symmetry. Some other representative symmetries to constrain the Berry curvature are discussed. See, for example, Ref. [10] and Ref. [11].
- [66] G. Kimbell, C. Kim, W. Wu, M. Cuoco, and J. W. Robinson, *Commun. Mater.* **3**, 19 (2022).
- [67] Q. Shao, Y. Liu, G. Yu, S. K. Kim, X. Che, C. Tang, Q. L. He, Y. Tserkovnyak, J. Shi, and K. L. Wang, *Nat. Electron.* **2**, 182 (2019).
- [68] Y. Cheng, S. Yu, M. Zhu, J. Hwang, and F. Yang, *APL Mater.* **9**, 051121 (2021).
- [69] G. Kimbell, P. M. Sass, B. Woltjes, E. K. Ko, T. W. Noh, W. Wu, and J. W. A. Robinson, *Phys. Rev. Mater.* **4**, 054414 (2020).
- [70] O. Busch, B. Göbel, and I. Mertig, *Phys. Rev. Res.* **2**, 033112 (2020).
- [71] M. N. Baibich, J. M. Broto, A. Fert, F. Nguyen Van Dau, F. Petroff, P. Etienne, G. Creuzet, A. Friederich, and J. Chazelas, *Phys. Rev. Lett.* **61**, 2472 (1988).
- [72] Y. Guo, J. Dai, J. Zhao, C. Wu, D. Li, L. Zhang, W. Ning, M. Tian, X. C. Zeng, and Y. Xie, *Phys. Rev. Lett.* **113**, 157202 (2014).
- [73] W. Butler, X.-G. Zhang, D. Nicholson, and J. MacLaren, *J. Magn. Magn. Mater.* **151**, 354 (1995).
- [74] E. J. Telford, A. H. Dismukes, R. L. Dudley, R. A. Wisconsin, K. Lee, D. G. Chica, M. E. Ziebel, M.-G. Han, J. Yu, S. Shabani *et al.*, *Nat. Mater.* **21**, 754 (2022).
- [75] S. H. Lee, Y. Zhu, Y. Wang, L. Miao, T. Pillsbury, H. Yi, S. Kempinger, J. Hu, C. A. Heikes, P. Quarterman, W. Ratcliff, J. A. Borchers, H. Zhang, X. Ke, D. Graf, N. Alem, C. Z. Chang, N. Samarth, and Z. Mao, *Phys. Rev. Res.* **1**, 012011(R) (2019).
- [76] J. Yan, X. Luo, F. C. Chen, Q. L. Pei, G. T. Lin, Y. Y. Han, L. Hu, P. Tong, W. H. Song, X. B. Zhu *et al.*, *Appl. Phys. Lett.* **111**, 022401 (2017).
- [77] P. Park, Y.-G. Kang, J. Kim, K. H. Lee, H.-J. Noh, M. J. Han, and J.-G. Park, *npj Quantum Mater.* **7**, 1 (2022).
- [78] E. Liu, Y. Sun, N. Kumar, L. Muechler, A. Sun, L. Jiao, S.-Y. Yang, D. Liu, A. Liang, Q. Xu *et al.*, *Nat. Phys.* **14**, 1125 (2018).
- [79] H. Hayashi, A. Asami, and K. Ando, *Phys. Rev. B* **100**, 214415 (2019).